Chapter 4

MnBi/Fe_3C@C nanocomposites

Chapter 4: MnBi/Fe_3C@C nanocomposites

4.1. Introduction

The low temperature phase of i.e. LTP MnBi is sought as a probable gap magnet without any rare earth elements. Ball milling is a promising technique for preparing MnBi magnets, however as our previous results showed, it has certain lacunas. It was discussed in our previous chapter that ball milling for more than 2 h at room temperature causes the decomposition of desired LTP phase. This decomposition increases the presence of a secondary phases Mn and (Bi), which are non-ferromagnetic and malleable. Consequently, due to Bi phase, reduction of the size of the low temperature phase becomes challenging. Hence, overall magnetization decreases with increased milling duration. In fact, lower magnetization values is an inherent challenge in Mn-Bi system.

To address this issue of phase breakdown during ball milling, cryo-milling has been adopted. This technique reduces the overall milling time required to achieve similar particle size reduction. Additionally, the cryogenic temperature slows down the occurrence of phase breakdown and potential oxidation that generally happen during milling at room temperature. Secondly, the low magnetization values were addressed, as suggested by Kneller and Hewig, by the preparation of exchange-spring magnets, which comprise of a magnetically hard phase and a soft phase, where exchange interaction results in enhanced energy product. Thus, the feasibility of utilizing Fe_3C@C as a soft phase in hard-soft composites was explored In this study, $Mn_{55}Bi_{45}$/Fe_3C@C nanocomposites with enhanced magnetic properties were prepared using cryogenic ball milling.

So far there has been limited exploration of alternative soft materials, such as ceramic Fe_3C@C, in the synthesis of hard-soft composites (e.g. MnBi). As part of the synthesis process, the application of a carbon coating on the MnBi grains is anticipated to enhance its saturation magnetization [1]. The structural and magnetic properties of these nanocomposites are thoroughly examined under cryogenic and room-temperature ball milling conditions.

4.2. Results and Discussion

Figure 4.1(a) depicts the powder x-ray diffraction of Fe_3C@C powder. The sharp crystalline peaks of the diffraction pattern were matched and indexed according to the JCPDS file no: 64-2413. The diffraction pattern confirmed the presence of a pure orthorhombic single phase along with carbon (26.3º). The average crystallite size of the powder calculated using Scherrer's equation. The crystallite size was found to be ~10 nm. Figure 1(b) shows the x-ray diffraction patterns of the pure $Mn_{55}Bi_{45}$ homogenised powder before milling and cryo-milled nanocomposites of MnBi and Fe_3C@C (0, 5, 10, 15 and 20 wt.%). The XRD patterns for the last three nanocomposites also displayed the presence of Fe_3C along with MnBi and Bi phases.

The as-cast and heat-treated alloy shows the presence of Bi-phase along with the desired LTP MnBi because of the incomplete peritectic reaction [1]. The heat treatment at 573 K for 24 h was done to enhance the LTP MnBi phase formation, which was evident from the relative increase in the peak intensity of LTP. The x-ray diffraction patterns for room temperature milled nanocomposites of MnBi and Fe_3C@C (0, 10, 15 and 20 wt.%) are shown in figure 1 (c). The three phases (*viz.* MnBi, Bi and Fe_3C) are evident from the XRD patterns. Earlier reports suggest that the desired LTP phase decomposes during milling process and results into an increased Bi phase [2]. This can be evidenced as a slight increase in the Bi and

Mn phase volume fractions of the milled samples in comparison to that of the homogenised sample (figures 4.1 b and c). In contrast, the MnBi system cryo-milled for 2 h had relatively higher content of LTP (figure 4.1 b). Further, in cryo-milled nanocomposites, with Fe_3C@C addition, the relative intensity of LTP to Bi peaks increased up to 10 wt. % and then decreased. On the other hand, the room temperature milled samples shown an increase in relative LTP intensity to Bi peak intensity with an increase in Fe_3C@C percentage. The possible explanation for this trend could be the increasing percentage of Fe_3C@C obstructing the LTP MnBi decomposition into Mn and Bi during milling. Also, room temperature milling causes the mechanically alloying of elemental Mn and Bi to form LTP MnBi causing an increase in the LTP to Bi peak intensity ratio. Additionaly, for cryo-milled samples, the relative ratio of LTP to Bi is higher till 10 wt.% additions of Fe_3C@C is because the cryogenic temperatures slow down the LTP decomposition.

However, the mechanical alloying is also sluggish at such lower temperatures ruling out the further formation of LTP. Moreover, the ratio of intensities of LTP/Bi for room temperature milled samples was always lesser than the cryo-milled ones. In addition, milled samples exhibit peak broadening, indicating size reduction and lattice strain during the milling process. The scherrer's equation was utilized for calculating the average crystallite size of near spherical Fe_3C@C particles. Since lattice strain is involved in milled samples, the Williamson Hall plot, was used to determine average crystallite size of the ball milled and cryo-milled $Mn_{55}Bi_{45}$ powder, which was found to be around 28 and 142 nm respectively. The variation in the average lattice strain values with milling duration can be seen in figure 4.1 (d). It depicts that the lattice strain is more in case of room temperature ball milled samples.

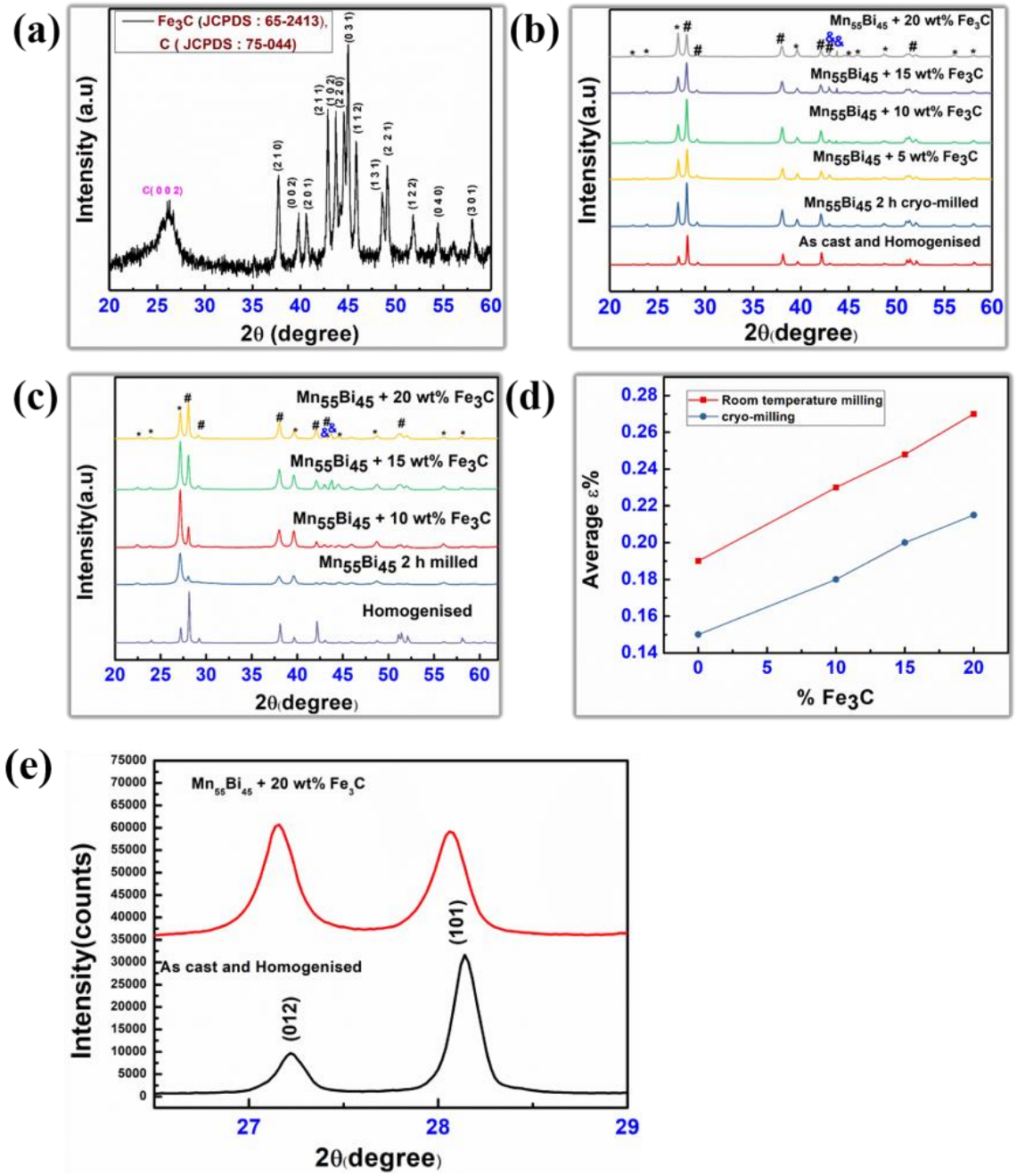

Figure 4.1. X-ray diffraction patterns of (a) Fe_3C@C nanoparticles, (b) $Mn_{55}Bi_{45}$ homogenised powder, $Mn_{55}Bi_{45}$ with 0, 10, 15, 20 wt.% of Fe_3C@C after 2 h cryo-milling added nanocomposites (c) $Mn_{55}Bi_{45}$ homogenised powder, $Mn_{55}Bi_{45}$ with 0, 10, 15, 20 wt.% of Fe_3C@C after 2 h of room temperature milling. (*-Bi phase, #- LTP MnBi phase, &- Fe_3C@C, ((hkl) indexing is similar to Figure 3.1 and not marked for better comprehensibility) (d) Calculated average lattice strain values for milled samples and (e) Magnified view of before and after cryo-milling depicting peak broadening.

Figure 4.2 shows the scanning electron micrographs (SEM), particle size distribution and compositional analysis of cryo-milled powders of $Mn_{55}Bi_{45}$. They reveal that cryo-milling results in finer polycrystalline particles, which agglomerate to form larger particles. It is also clear from the high-magnification micrographs that these particles are random in shape (Fig. 4.2a).

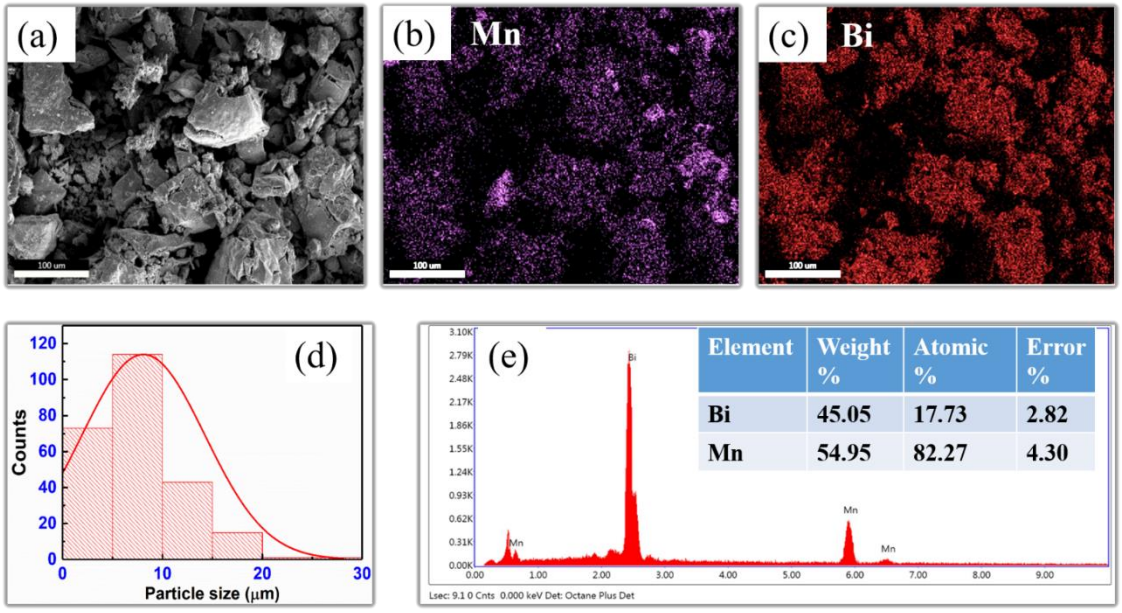

Figure 4.2. (a) Scanning electron micrograph of cryo-milled $Mn_{55}Bi_{45}$ powder and its corresponding elemental mapping for (b) for Mn, (c) Bi, (d) particle size distribution and (e) Energy Dispersive x-ray Spectroscopic analysis.

The elemental composition was confirmed from the energy dispersive x-ray spectroscopy (EDS) attachment of the SEM as seen in the inset of Figure 4.2e. The distribution of constituents (Mn and Bi) can also be seen as uniform throughout the sample (Figure 2b & 2c). The particle size distribution was estimated from the micrograph using Image J software [3]. Based on the XRD and SEM results, it can be understood that cryo-

milling is effective in reducing the $Mn_{55}Bi_{45}$ average particle size to the range of 6.6 ± 0.16 μm in 2 h (Figure 4.2d).

Figure 4.3 shows the SEM micrographs and EDS elemental mapping of the MnBi/ Fe_3C@C (10 wt.%) nanocomposite. The average particle size of the cryo-milled nanocomposite calculated from the SEM micrograph (Figure 3a) can be seen in Figure 4.3d. It was found to be 1.47± 0.02 μm after 2 h of milling. The compositional mapping obtained through the EDS attachment of SEM shows a uniform distribution of elements with certain regions of Mn concentration. Further, the formation of elemental Bi as a consequence of LTP decomposition during milling is also minimized. This is due to the slowing of the decomposition kinetics at sub-zero temperatures. Additionally, the oxidation of particles reported during room temperature milling in other studies is almost diminished due to reduced kinetics at sub-zero temperature.

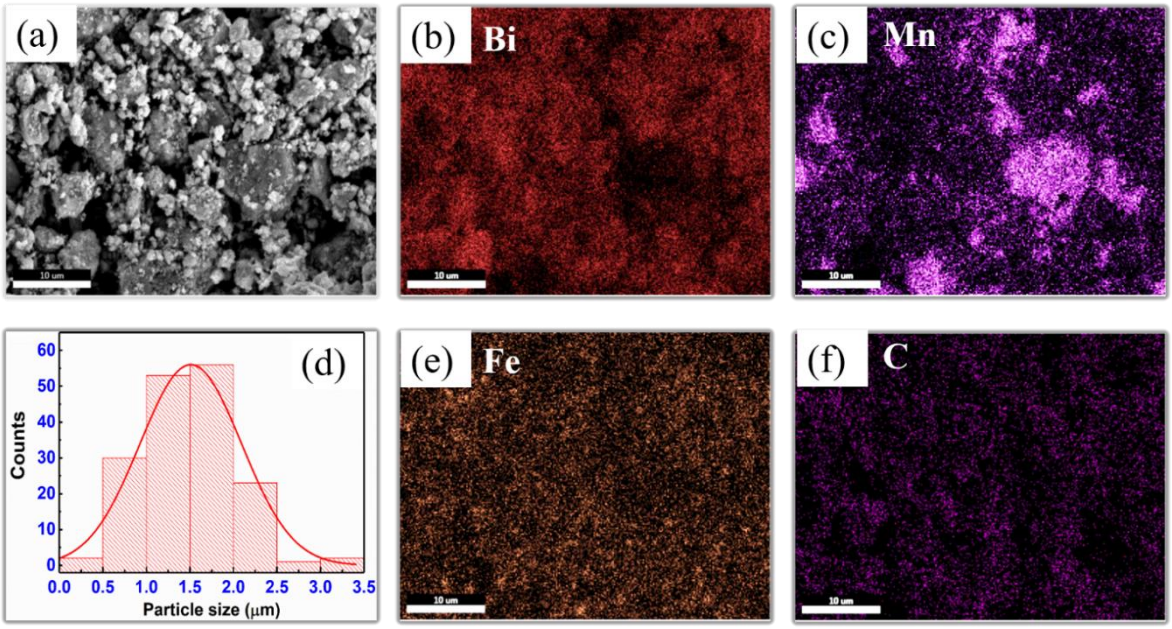

Figure 4.3. (a) Scanning electron micrograph of cryo-milled MnBi/Fe_3C@C (10 wt.%) nanocomposite powder and its corresponding elemental mappings (b) Bi, (c) Mn, (e) Fe, (f)C and (d) particle size distribution.

Further, to evaluate the particle size and morphology, transmission electron microscopy was performed for Fe_3C@C nanoparticles. As shown in the bright-field image, figure 4.4 (a), the Fe_3C@C nanoparticles have different shapes i.e., some of them are spherical while others are distorted spherical. Irrespective of the shape of the particles, the bright field image reveals a fine greyish contrast coating around all the dark particles. Inset of Fig. 4a shows a magnified image of the outer region of the particles confirming the coating. ImageJ software was used to calculate the average particle size from the bright field image which was 154 (±19) nm and the coating thickness was around 2-5 nm. The interplanar spacing calculated from the HRTEM image using Image J software matched with that of (0 0 2) plane of orthorhombic Fe_3C.

Further, figure 4.4(c) shows the bright field image of MnBi/Fe_3C@C (10 wt.%) nanoparticles. The different contrast of particles is due to their existence as different class of materials i.e. the former is intermetallic and the latter one is ceramic. The nanocomposite displayed agglomeration, which is commonly observed for milled samples. Nevertheless, the agglomeration is further enhanced due to nanostructured and magnetic nature. Figure 4.4 (c) depicts the spherical Fe_3C@C particle interacting with the MnBi particle through the C-coating over the former. This coating (~ 2-5 nm) might have facilitated the tunnelling of electrons with spins through it which might have supported the exchange coupling amongst the two phases. From Figure 4.4 (c), the MnBi and Fe_3C@C were distinguished based on the size, shape as well as carbon coating. The Fe_3C@C particles are of smaller dimension, nearly spherical in shape and have coating of carbon on their surface. Similar coating of carbon over pure and substituted Fe_3C was also reported in the earlier work of our group [4-6]. The

corresponding diffraction pattern confirms the presence of LTP MnBi, Bi and Fe_3C@C phases in the nanocomposite (Fig. 4.4d).

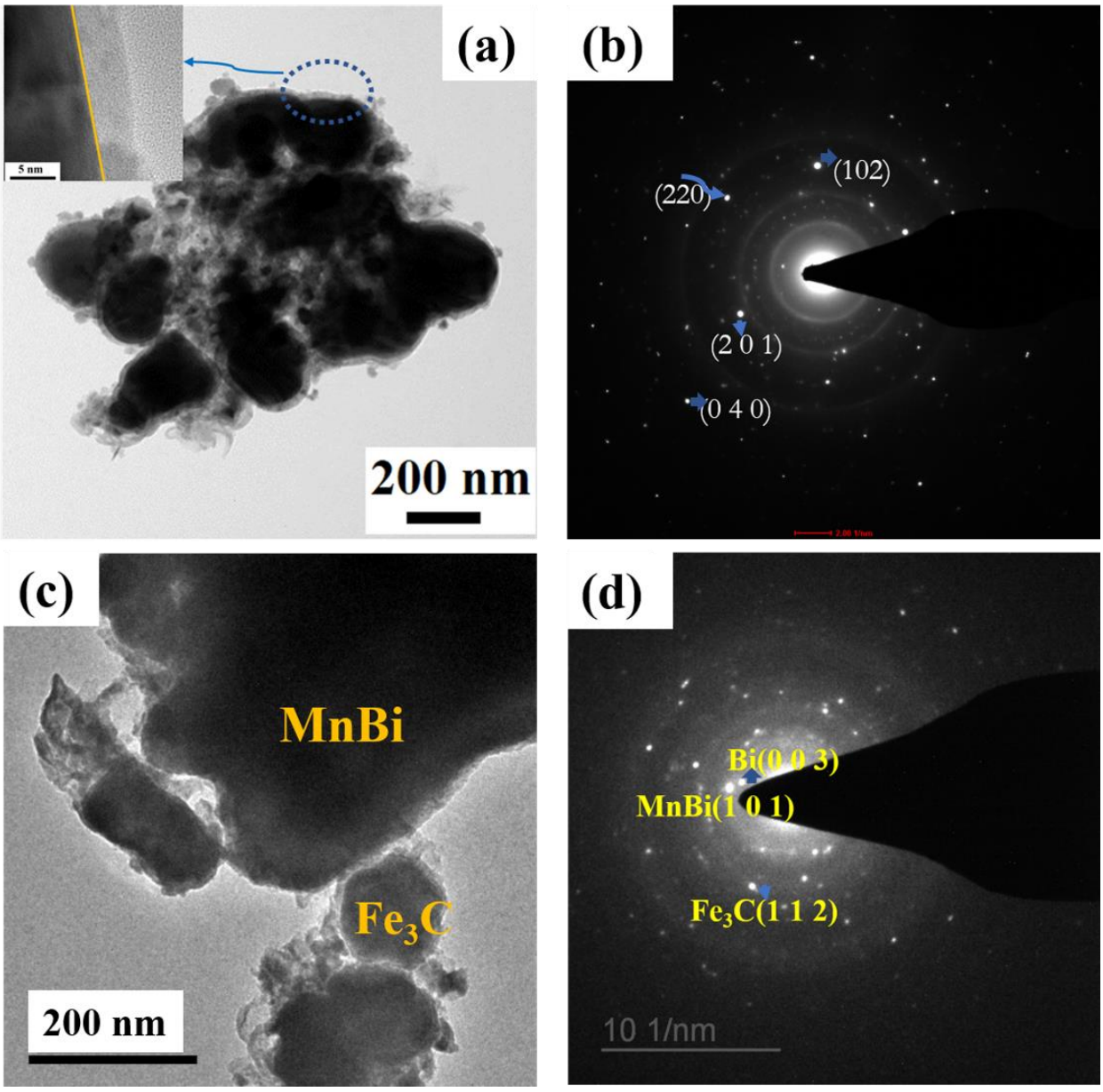

Figure 4.4.(a) Bright-field image and (b) corresponding diffraction pattern of orthorhombic Fe_3C@C nanoparticles (c) Bright field image and (d) corresponding diffraction pattern of nanocomposites of MnBi/ Fe_3C@C (10 wt.%).

To further understand the nano-coating found around the Fe3C nanoparticles in the TEM brigh field images, high-angle annular dark field (HAADF) was performed (Figure 4.5). The HAADF elemental mapping clearly shows the coating observed in Figure 4a was that of carbon, as shown in Figure 4.5c. The coating, mapped green can be seen to be that of carbon in HAADF imaging.

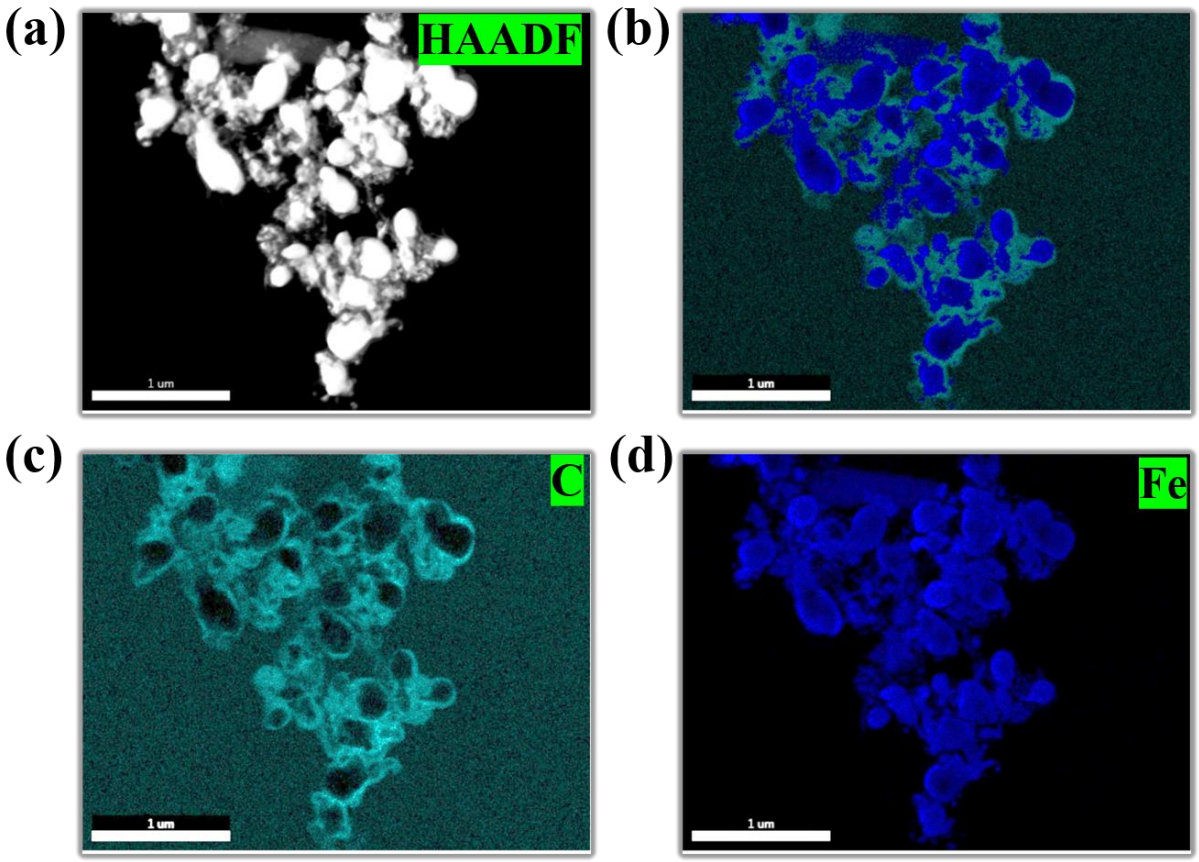

Figure 4.5. (a) High-angle annular dark field image of Fe_3C@C nanoparticles and its corresponding elemental mappings (b) overall, (c) C and (d) Fe.

The formation of Fe_3C@C could have occurred due to the carburization of Fe_3O_4. In this process, ethylenediamine was used as a reducing agent, which evaporates with the increased temperature and fills the chamber of the alumina tube. This gas further carburizes Fe_3O_4

initially into Fe_5C_2 and, with a subsequent rise in temperature (above 620°C), finally forms Fe_3C. The excess carbon gets coated over Fe_3C. The inert N_2 gas flow rate was kept sufficiently slow such that the evaporated ethylenediamine gets sufficient reaction time to reduce [7].

Figure 4.6 depicts the M *vs.* H loops at room temperature for Fe_3C@C nanoparticles and homogenised MnBi alloy. The M_S value for Fe_3C@C nanoparticles was ~ 150 emu/g whereas its M_r and H_C values were 4.35 emu/g and 79 Oe respectively (figure 4.6a). It can be observed that saturation magnetization values were greater than the bulk Fe_3C (~140 emu/g) that could be achieved. This high M_S value could be attributed to the fine-uniform carbon coating on the surface of the Fe_3C nanoparticles. Such behaviour has also been reported by Gangwar et al. for (α-Mn_3O_4/MnO)@rGO nanoparticle where, α-Mn_3O_4/MnO has paramagnetic nature at room temperature but behaves as ferrimagnetic (M_S = 7.1 emu/g) after getting coated with r-GO [8]. Moreover, the M_S value obtained for the present sample is quite higher than that of the other reported values (~ 70-115 emu/g) [9-10]. For the present case the Fe_3O_4 used for the preparation of Fe_3C@C was prepared using a solvothermal process had size ~ 210 nm [3-4]. As a result, the obtained Fe_3C@C was also bigger in dimension than the earlier reported samples [3-4], leading to obvious greater M_S value.

Figure 4.6(b) displays the M *vs*. H loop of the as cast and homogenised (at 300 K for 24 h) $Mn_{55}Bi_{45}$ alloy at room temperature. The homogenised sample, at room temperature, displayed a coercivity of around 570 Oe with M_S and M_r values of 58.6 and 13 emu/g respectively. The theoretically calculated M_S value of LTP-MnBi phase is 83 emu/g thus the present homogenised alloy has 70.6% of the theoretical M_S value [11]. This variation in

values could be due to two factors. Primarily, the homogenized alloy also contained a paramagnetic Bi phase along with the desired LTP, as can be seen from the XRD pattern as shown in Figure 1. In addition, certain Mn atoms can occupy the interstitial voids of LTP (NiAs structure) and can cause antiferromagnetic interactions, which in turn, cause a reduction in M_S values[12].

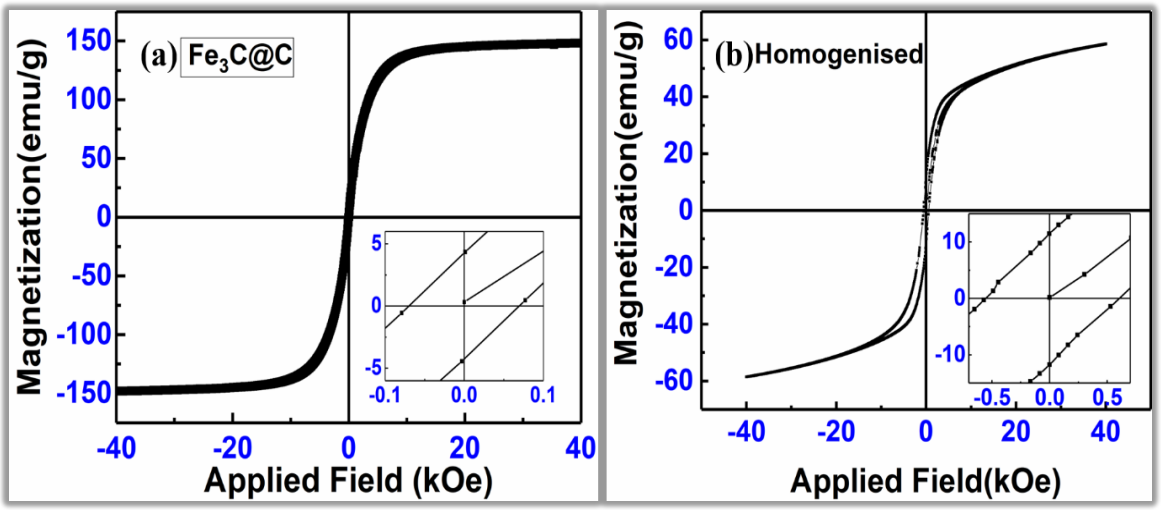

Figure 4.6. Room temperature M *vs*. H hysteresis loops under ± 40 kOe of (a) Fe_3C@C nanoparticles and (b) homogenized $Mn_{55}Bi_{45}$ powder.

Figure 4.7 refers to the hysteresis loops of the cryo-milled samples. Since coercivity is an extrinsic parameter and sensitive to microstructure, cryo-milling was done for 2 h to refine the particle size. In addition, room-temperature high-energy ball milling was also performed under same parameters and their hysteresis loops have been recorded for comparison. The durations for cryogenic and room temperature milling were chosen such that the LTP decomposition could be minimal.

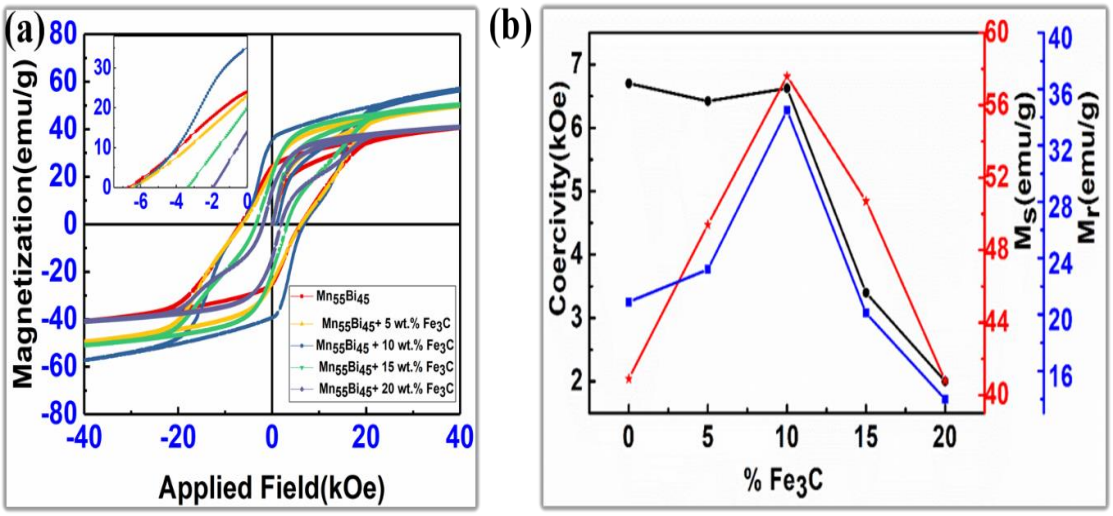

Figure 4.7. M *vs*. H hysteresis loops of cryo-milled powders of (a)$Mn_{55}Bi_{45}$ with 5, 10, 15 and 20 wt. % of Fe_3C@C and (b) variation of magnetic properties of cryo-milled nanocomposites with varying Fe_3C@C addition to $Mn_{55}Bi_{45}$.

It can be observed from Figure 4.7 that the milled powders ($Mn_{55}Bi_{45}$ with 0, 10, 15 or 20 wt.% of Fe_3C@C) exhibit better coercivities. This is due to the reduction in particle size, which was evident from their XRD patterns shown in Fig. 4.2. The pure cryo-milled $Mn_{55}Bi_{45}$ powder displayed a M_S value of 40.9 emu/g whereas its M_r and H_C values were around 20.9 emu/g and 6.7 kOe respectively. It was observed that upon the addition of soft phase (Fe_3C@C) up to 10 wt. % there was an increase in the M_S and M_r values without much change in the H_C values. The 10 wt. % nanocomposite displayed the optimum values with H_C of 6.6 kOe, M_S ~ 57 emu/g and M_r ~35 emu/g. These values observed are much better than the reported magnetization values of other room temperature milled MnBi samples (Figure 4.7) [13]. The most common signature of "Kinks" found in the M vs H loops of pure

Mn-Bi milled samples in literature can also be seen in Figure 4.7 and 4.8. It is to be noted that even pure milled $Mn_{55}Bi_{45}$ powders displayed a step/kink in their hysteresis loops. These kinks are mainly attributed to the presence of different sized particles or to the presence of different phases [2, 13]. Since, for the present nanocomposites, the magnetic values were higher than the values obtained from the simple rule of mixtures. This suggests the presence of exchange interaction between the hard and soft magnetic phases. Thus, the kinks observed for the nanocomposite are not due to poor exchange coupling. It might be because of presence of different sized particles. Further, this exchange interaction was possibly due to the tunnelling of magnetic spins through C thin layer between the two phases (Figure 4.4 and 4.5). Even recent first principle calculations and experimental studies suggest that carbon has positive impact on MnBi magnetization [14]. The lowering of coercivity at higher than 10 wt.% and increase in M_r values validate the interaction between MnBi and Fe_3C@C.

The coercivity alsodecreased as the content of the soft phase increased above 10 wt. %. Whenever the demagnetizing field reverses the moments in some grains of Fe_3C@C, the exchange interaction also reverses the moments in the adjacent grains of the hard hexagonal MnBi phase. Due to the neighboring moments in hard/soft systems, an additional demagnetizing field decreases the H_C of nanocomposites [15-16]. However, the lower M_r values can be ascribed to the fact that the nano-crystalline particles exhibit a magnetic behavior that is isotropic. Concurrently, the M_r/M_S ratio is only 0.5 in such cases [17]. Due to the mentioned reasons for lowering of M_r values, the energy product of the 10 wt. % nanocomposite was calculated to be 2 MGOe, considerably higher amongst the other reports on isotropic powder [2]. However, literature suggests that the energy product of the hard

magnets considerably enhances after a magnetic field alignment. Further addition of the soft phase led to the reduction in both H_C and M_S values, as shown in Figures 4.7 and 4.8.

It was observed for the room temperature milled samples, as seen in Figure 4.8, that they exhibit lower H_C and M_S values than their cryo-milled counter parts. Though M_S and M_r values linearly increased up to 43 emu/g as shown in Figure 8 (a) and (b), H_C drastically reduced with Fe_3C@C addition. This concludes that cryo-milling technique with 10 wt. % Fe_3C@C would provide better magnetic properties.

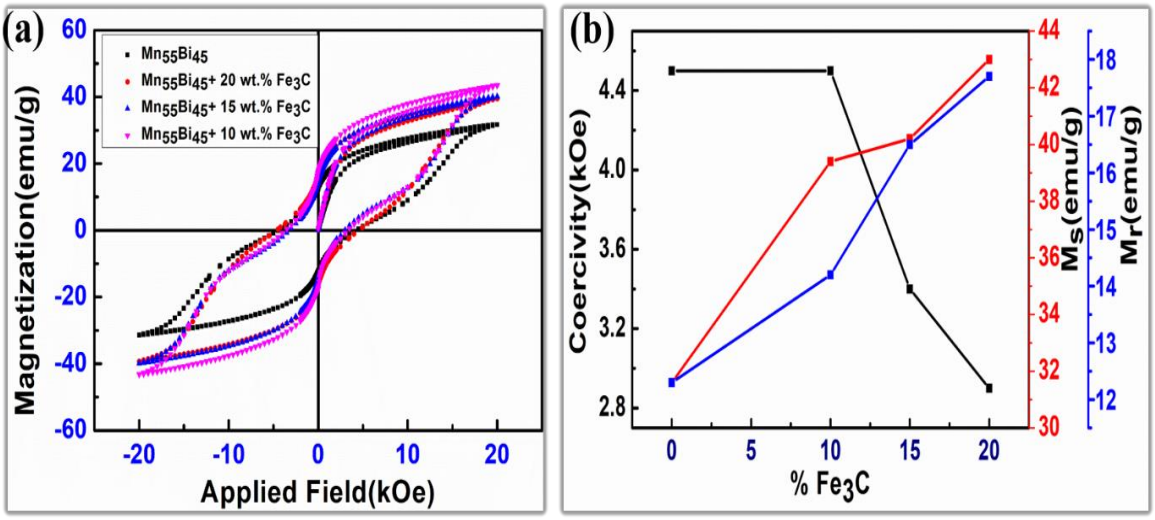

Figure 4.8. (a) M *vs*. H loops of the room temperature ball milled samples upto (± 20 kOe) and (b) variation of magnetic properties of room temperature milled nanocomposites with varying Fe_3C@C addition to $Mn_{55}Bi_{45}$.

Plots of dM/dH vs. H, as shown in the Fig. 4.9, allows to qualitatively understand the degree of exchange coupling between hard-soft phases. Narrow peaks at high negative fields are correlated with strong exchange and narrow crystallite grain distribution [18-19].

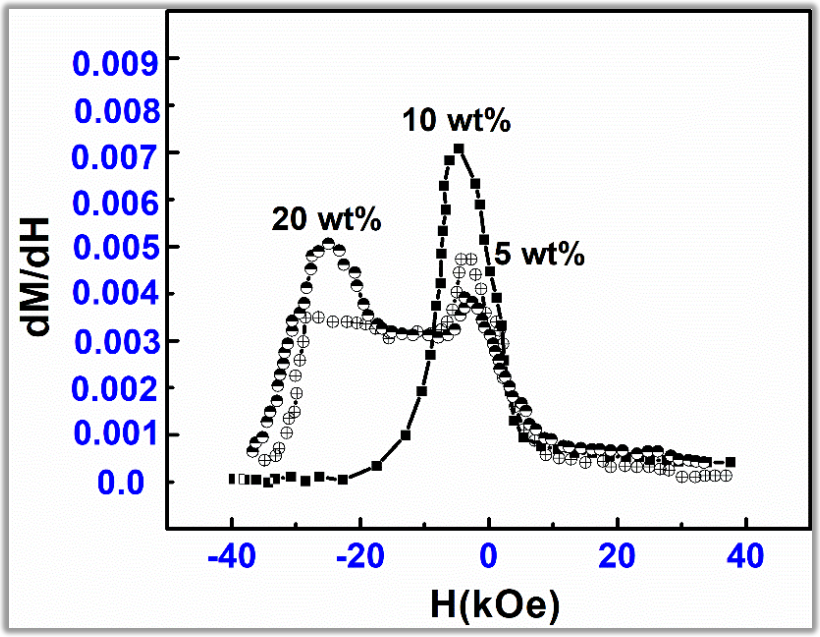

Figure 4.9. Switching field distribution curves of cryomilled nanocomposites with 5,10 and 20 wt.% Fe_3C@C addition.

It is also evident from the SFD (switching field distribution) curve that good exchange coupling between the hard and soft phases exists when the soft phase was 10 wt.% as it exhibited a single smooth loop. Since two distinct maxima are expected for an uncoupled hard and soft phase mixture, the presence of a secondary narrow maximum at a low field for 5 and 20 wt% samples suggests that a portion of the hard and soft grains were not exchange coupled [20].

4.3. Conclusions:

Fe_3C@C nanoparticles were successfully synthesized that was confirmed through XRD and TEM measurements. The carbon coating applied to the nanoparticles resulted in relatively higher magnetization values (~150 emu/g). MnBi/Fe_3C@C nanocomposites were prepared using both cryo-milling and room temperature milling techniques. Comparative analysis revealed that the cryo-milled samples exhibited superior properties, particularly the nanocomposite with a 10 wt. % addition of Fe_3C@C, which demonstrated a H_C value of 6.6 kOe, M_S value of 57 emu/g, and M_r value of 35 emu/g. The feasibility of incorporating Fe_3C@C as a soft phase in MnBi nanocomposites to enhance the overall energy product has been established. The presence of a nanolayer of carbon could have facilitated the exchange coupling between MnBi and Fe_3C through spin tunneling. Notably, Fe_3C@C contributed to the composite's high initial magnetization value, while the carbon component improved its oxidation resistance, as no oxide phases were observed in the composites. Consequently, Fe_3C@C emerged as a promising candidate for a soft magnetic phase in the development of exchange-coupled magnets alongside other hard magnetic materials.

4.4. References

1. Z. Xiang, T. Wang, S. Ma, L. Qian, Z. Luo, Y. Song, H. Yang, W. Lu, Microstructural evolution and phase transformation kinetics of MnBi alloys, J. Alloys Compd. 741 (2018) 951–956.
2. N.V.R. Rao, A.M. Gabay, W.F. Li, G.C. Hadjipanayis, Nanostructured bulk MnBi magnets fabricated by hot compaction of cryomilled powders, J. Phys. D. Appl. Phys. 46 (2013) 265001.
3. C.A. Schneider, W.S. Rasband, K.W. Eliceiri, NIH Image to ImageJ: 25 years of image analysis, Nat. Methods. 9 (2012) 671–675.
4. A. Gangwar, S.S. Varghese, S.S. Meena, C.L. Prajapat, N. Gupta, N.K. Prasad, Fe3C nanoparticles for magnetic hyperthermia application, J. Magn. Magn. Mater. 481 (2019) 251–256.
5. Gangwar, S.K. Alla, M. Srivastava, S.S. Meena, E. V Prasadrao, R.K. Mandal, S.M. Yusuf, N.K. Prasad, Structural and magnetic characterization of Zr-substituted magnetite ($Zr_xFe_{3-x}O4$, $0\leq x\leq 1$), J. Magn. Magn. Mater. 401 (2016) 559–566.
6. Gangwar, G. Singh, S.K. Shaw, R.K. Mandal, A. Sharma, S.S. Meena, C.L. Prajapat, N.K. Prasad, Synthesis and structural characterization of $Co_xFe_{3-x}C$ ($0\leq x\leq 0.3$) magnetic nanoparticles for biomedical applications, New J. Chem. 43 (2019) 3536–3544.
7. X. Lei, W. Wang, Z. Ye, N. Zhao, H. Yang, High saturation magnetization of Fe3C nanoparticles synthesized by a simple route, Dye. Pigment. 139 (2017) 448–452.
8. A. Gangwar, S.K. Shaw, A. Sharma, S.K. Alla, S. Kavita, M. Vasundhara, J. Gupta, K.C. Barick, P.A. Hassan, N.K. Prasad, Ferrimagnetic (α-Mn3O4/MnO)@ rGO

nanocomposite as potential adsorbent for organic pollutant dye, Appl. Surf. Sci. 612 (2023) 155778.

9. Z. Ye, Y. Qie, Z. Fan, Y. Liu, H. Yang, Exchange-coupled of soft and hard magnetic phases on the interfaces of Fe3C/CoFe2O4 nanocomposites, Ceram. Int. 46 (2020) 731–736.
10. M. Peng, Y. Qiao, M. Luo, M. Wang, S. Chu, Y. Zhao, P. Liu, J. Liu, Y. Tan, Bioinspired Fe3C@ C as highly efficient electrocatalyst for nitrogen reduction reaction under ambient conditions, ACS Appl. Mater. Interfaces. 11 (2019) 40062–40068.
11. J. Liu, B. Yu, Q. Zhang, L. Hou, Q. Huang, C. Song, S. Wang, Y. Wu, Y. He, J. Zou, Synthesis and magnetic properties of Fe3C–C core–shell nanoparticles, Nanotechnology. 26 (2015) 85601.
12. J. Yang, W. Yang, Z. Shao, D. Liang, H. Zhao, Y. Xia, Y. Yang, Mn-based permanent magnets, Chinese Phys. B. 27 (2018). https://doi.org/10.1088/1674-1056/27/11/117503.
13. S.K. Sharma, D. Pradhan, S. Ram, A core–shell magnet Mn70Bi30 grown at seeds in magnetic fields and its impacts on its spin-dynamics, Curie point and other tailored properties, Nanotechnology. 34 (2023) 335703.
14. P. Kharel, B. Lama, M. Flesche, Z. Mehlberg, B. Lamsal, S. Valloppilly, Y. Zhou, D.J. Sellmyer, T.R. Paudel, Modifying magnetic properties of MnBi with carbon: an experimental and theoretical study, J. Phys. D. Appl. Phys. 55 (2022) 265003.
15. S. Kavita, V. V Ramakrishna, A. Srinivasan, R. Gopalan, Structural and magnetic properties of the low temperature phase MnBi with ball milling, Mater. Res. Express. 3 (2016) 56102.

16. H. Nikmanesh, M. Moradi, P. Kameli, G.H. Bordbar, Effects of annealing temperature on exchange spring behavior of barium hexaferrite/nickel zinc ferrite nanocomposites, J. Electron. Mater. 46 (2017) 5933–5941.
17. Y.L. Ma, X.B. Liu, K. Gandha, N. V Vuong, Y.B. Yang, J.B. Yang, N. Poudyal, J. Cui, J.P. Liu, Preparation and magnetic properties of MnBi-based hard/soft composite magnets, J. Appl. Phys. 115 (2014) 17A755.
18. Rong, H. Zhang, R. Chen, S. He, B. Shen, The role of dipolar interaction in nanocomposite permanent magnets, J. Magn. Magn. Mater. 302 (2006) 126–136.
19. B.K. Rai, S.R. Mishra, Magnetically enhanced hard–soft SmCo5–FeNi composites obtained via high energy ball milling and heat treatment, J. Magn. Magn. Mater. 344 (2013) 211–216.
20. J. Zhang, S. Zhang, H. Zhang, B. Shen, Structure, magnetic properties, and coercivity mechanism of nanocomposite SmCo 5/α-Fe magnets prepared by mechanical milling, J. Appl. Phys. 89 (2001) 5601–5605.